Structure

Article

D-loop Dynamics and Near-Atomic-Resolution Cryo-EM Structure of Phalloidin-Bound F-Actin

Graphical Abstract

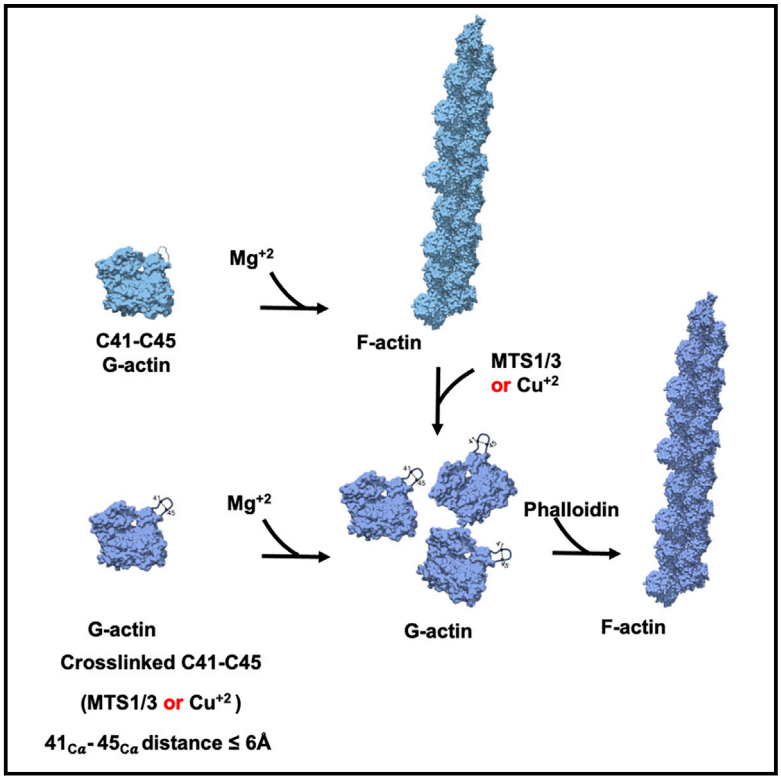

Authors

Sanchaita Das, Peng Ge, Zeynep A. Oztug Durer, Elena E. Grintsevich, Z. Hong Zhou, Emil Reisler

Correspondence

reisler@mbi.ucla.edu

In Brief

Actin plays crucial roles in biological systems and its DNase 1 binding loop interacts with several actin-binding proteins. Das et al. demonstrate that phalloidin (phallotoxin) "glues" the two strands of actin filaments through additional contacts between protomers.

Highlights

- Structure-function insights into actin as revealed by cryo-EM and light scattering
- D-loop dynamics and its effect on filament assembly and stability
- Phalloidin rescues the assembly of defective crosslinked G-actin D-loop mutant
- Phalloidin stabilize the actin assembly by allowing inter-protomer D-loop

Das et al., 2020, Structure *28*, 586–593
May 5, 2020 © 2020 Elsevier Ltd.
https://doi.org/10.1016/j.str.2020.04.004

CellPress

CellPress

Structure

Article

D-loop Dynamics and Near-Atomic-Resolution Cryo-EM Structure of Phalloidin-Bound F-Actin

Sanchaita Das,[1] Peng Ge,[2] Zeynep A. Oztug Durer,[1,5] Elena E. Grintsevich,[1,6] Z. Hong Zhou,[2,3,4] and Emil Reisler[1,4,7,*]
[1]Department of Chemistry and Biochemistry, University of California, UCLA, Los Angeles, CA 90095, USA
[2]California NanoSystems Institute (CNSI), UCLA, Los Angeles, CA 90095, USA
[3]Department of Microbiology, Immunology and Molecular Genetics, UCLA, Los Angeles, CA 90095, USA
[4]Molecular Biology Institute, UCLA, Los Angeles, CA 90095, USA
[5]Present address: Department of Biophysics, School of Medicine, Acibadem MAA University, Istanbul, Turkey
[6]Present address: Department of Chemistry and Biochemistry, California State University, Long Beach (CSULB), CA 90840, USA
[7]Lead Contact
*Correspondence: reisler@mbi.ucla.edu
https://doi.org/10.1016/j.str.2020.04.004

SUMMARY

Detailed molecular information on G-actin assembly into filaments (F-actin), and their structure, dynamics, and interactions, is essential for understanding their cellular functions. Previous studies indicate that a flexible DNase I binding loop (D-loop, residues 40–50) plays a major role in actin's conformational dynamics. Phalloidin, a "gold standard" for actin filament staining, stabilizes them and affects the D-loop. Using disulfide crosslinking in yeast actin D-loop mutant Q41C/V45C, light-scattering measurements, and cryoelectron microscopy reconstructions, we probed the constraints of D-loop dynamics and its contribution to F-actin formation/stability. Our data support a model of residues 41–45 distances that facilitate G- to F-actin transition. We report also a 3.3-Å resolution structure of phalloidin-bound F-actin in the ADP-Pi-like (ADP-BeFx) state. This shows the phalloidin-binding site on F-actin and how the relative movement between its two protofilaments is restricted by it. Together, our results provide molecular details of F-actin structure and D-loop dynamics.

INTRODUCTION

Actin dynamics, polymerization, depolymerization, and the remodeling of its assembled forms play a key role in many cellular processes (Neuhaus et al., 1983). Thus, a detailed molecular and structural description of the mechanisms that regulate actin structures is essential for understanding its cellular interactions and functions. The structural flexibility and mobility of some of its domains is evident in numerous atomic-resolution structures of G-actin (Kabsch et al., 1990; Dominguez and Holmes, 2011; Pollard, 2016, 2017). Normal mode analysis attributes such movements to loop elements in subdomains of actin, such as its DNase I binding loop (D-loop; residues 40–50), hydrophobic loop (H-loop; residues 264–273), C-terminus (including residues 374 and 375), and the W-loop (residues 165–172) (Tirion and ben-Avraham, 1993). Cysteine mutagenesis in combination with chemical crosslinking approaches has been utilized to document the innate flexibility of these subdomains in G- and F-actin (Kim and Reisler, 1996, Kim et al., 1998).

Several crystal structures of G-actin reveal disordered D-loop and C-terminus (Kim et al., 1998; Graceffa and Dominguez, 2003; McLaughlin et al., 1993; Robinson et al., 1999), suggesting their intrinsic flexibility. Other studies show that the D-loop can adopt different secondary conformations; a β strand in the actin complex with DNase I (Kabsch et al., 1990), a short α helix (Otterbein et al., 2001) in the crystal structure of ADP-actin, and a disordered form in the ATP-bound state (Graceffa and Dominguez, 2003). Molecular dynamics (MD) simulations of ATP- and ADP-G-actin suggest that the D-loop can transition to a helical structure (Zheng et al., 2007), but cysteine scanning mutagenesis paired with spin labeling (Durer et al., 2012) reveals that if it exists, this state is not predominant and may exist only transiently. Other studies also show a highly unstable nature of this helix in different nucleotide-bound states (Zheng et al., 2007; Dalhaimer et al., 2008; Saunders et al., 2014) and/or do not detect it at all (Rould et al., 2006).

Monomeric G-actin contains bound nucleotide (ATP) and divalent cation as cofactors. Actin polymerization is accompanied by ATP hydrolysis followed by the release of γ-phosphate (Pi) (Pollard, 2016). Some actin-binding proteins are reported to have different affinity toward different nucleotide-bound states of actin (Paavilainen et al., 2004). Previous studies suggest that ATP- and ADP-Pi-bound filaments are less flexible and more stable than ADP-bound F-actin (Orlova and Egelman, 1992, 1993), and that their severing by cofilin is attenuated (Suarez et al., 2011). A model of F-actin based on X-ray diffraction data suggests that the G- to F-actin transition involves: (1) domain movements in G-actin that facilitate F-actin formation; and (2) an open and extended D-loop conformation in F-actin (as compared with that in G-actin [Oda et al., 2009]). Recent advances in high-resolution cryoelectron microscopy (cryo-EM) investigations and biochemical studies provide snapshots of F-actin in its different states (Merino et al., 2018; Chou and Pollard, 2019; Galkin et al., 2015). They reveal differences in the conformation and location of the D-loop (Figure 1) and confirm its plasticity that was shown in previous publications

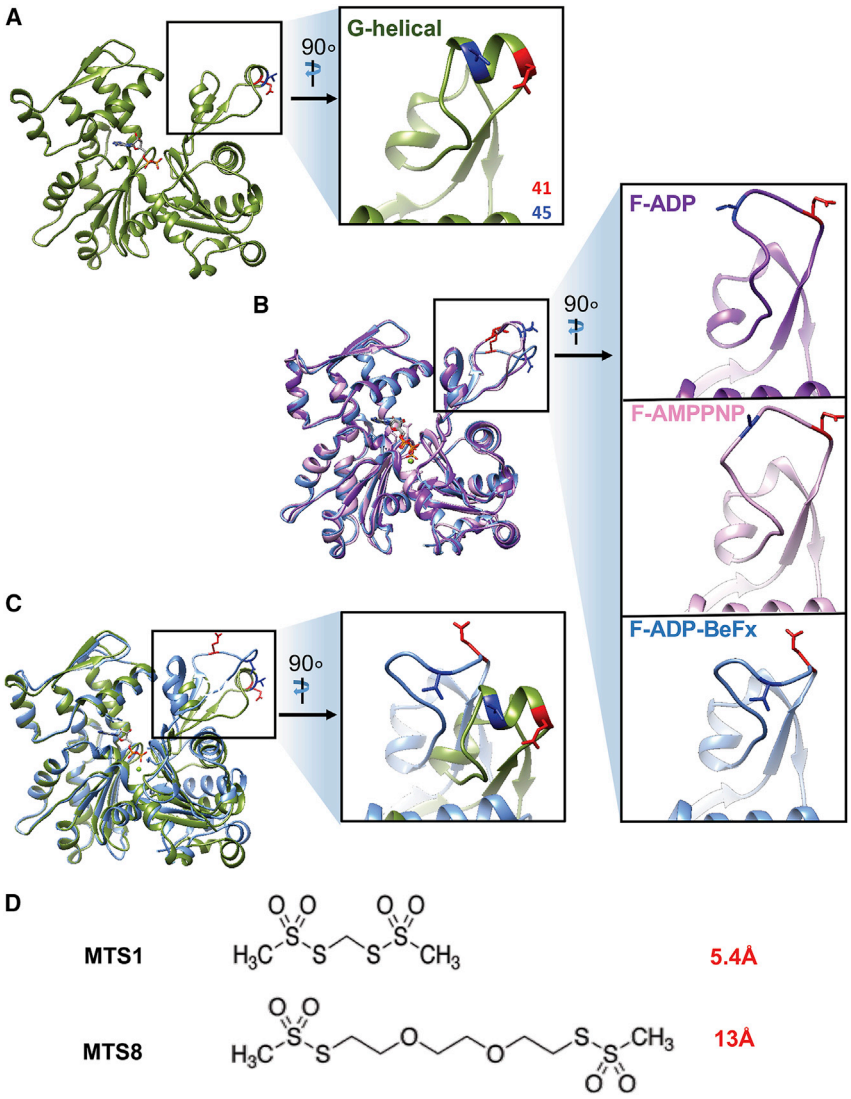

Figure 1. D-loop Flexibility Depends on the Nucleotide State of Actin

(A and B) Comparison of D-loops in different F-actin structures with a helical D-loop (PDB: 1J6Z) in G-actin (A). High-resolution cryo-EM structures of F-actin with the bound ADP (PDB: 6DJO), AMPPNP (PDB: 6DJM), and ADP + BeFx (PDB: 5OOF) show the corresponding loop states (B).

(C) Comparison of G-actin D-loop conformations in the helical state and in ADP-BeFx-F-actin. In both forms, residues 41 and 45 are marked in red and blue, respectively. For 90° rotated close-up images, some regions of actin structure have been clipped by Chimera for visual clarity.

(D) MTS1 and MTS8 reagents and their crosslinking distances.

(Oztug Durer et al., 2010; Durer et al., 2012; Kotila et al., 2018). High-resolution structures of F-actin with the various bound nucleotides also suggest that the Dloop helps in stabilizing inter-protomer contacts within the filament (Merino et al., 2018; Chou and Pollard, 2019). Conversely, D-loop perturbation, as in Mical oxidized actin, can lead to F-actin disassembly (Grintsevich et al., 2017). Notably, the toxin phalloidin compensates for D-loop-related polymerization defects by introducing additional inter-protomer contacts (Oda et al., 2005).

Clearly, the plasticity and conformational state of the D-loop affects the G- to F-actin transition. To test the filaments constraints on D-loop span/confirmation, we use a double-cysteine D-loop mutant Q41C/V45C of yeast actin (with a C374 mutation). We probe the effect of variable-length crosslinkings between these two residues on G- to F-actin transition and filament stability. A similar approach was used before to test the H-loop (amino acids 262–274) states in yeast F-actin and revealed that trapping the loop in a transient ''parked'' position (by crosslinking C180 to C269 with short-span reagents) disrupted the filaments (Shvetsov et al., 2006). In this study we also use negative-stain electron microscopy (NS-EM) and cryo-EM to obtain a structure, at 3.3-Å resolution, of F-actin-phalloidin in the ADP-Pi-like state (mimicked by ADP-BeFx), i.e., in the most stable form of actin filaments.

RESULTS

This study aims to probe D-loop plasticity and its importance in filament formation and stability. We utilized a double-cysteine mutant, C41/C45, which can be constrained by crosslinking to different widths. This allows us to assess the minimal C41-to-C45 distance that facilitates G- to F-actin transition. Additionally we observed that phalloidin, a common reagent used to stabilize F-actin, was able to overcome a polymerization defect that was caused by C41-C45 crosslinking in the D-loop mutant. This led us to obtain a near-atomic-resolution structure of actin bound to phalloidin and BeFx. Although the interaction of actin with phalloidin was mapped in a previous actomyosin structure publication (Mentes et al., 2018), we show here the actin-phalloidin complex structure without other proteins bound to it.

Crosslinking of C41 to C45 in Yeast Actin Mutant and Its Effect on Actin Assembly

Previous studies (Oztug Durer et al., 2010) indicated that single-residue yeast actin mutants Q41C and V45C had polymerization rates comparable with that of wild-type actin. These mutants' residues were also found to be involved in inter-protomer contacts by crosslinking them with C265 and C374 of neighboring subunits. Here, we utilize disulfide crosslinking between C41 and C45 of the D-loop double mutant to find out whether it affects G- to F-actin polymerization. The disulfide formation was catalyzed by addition of $CuSO_4$ to G- or F-actin. As monitored by light scattering and EM imaging, the crosslinked G-actin was unable to polymerize into filaments after addition of $MgCl_2$ (Figure S1). Addition of $CuSO_4$ to mutant F-actin destroyed the

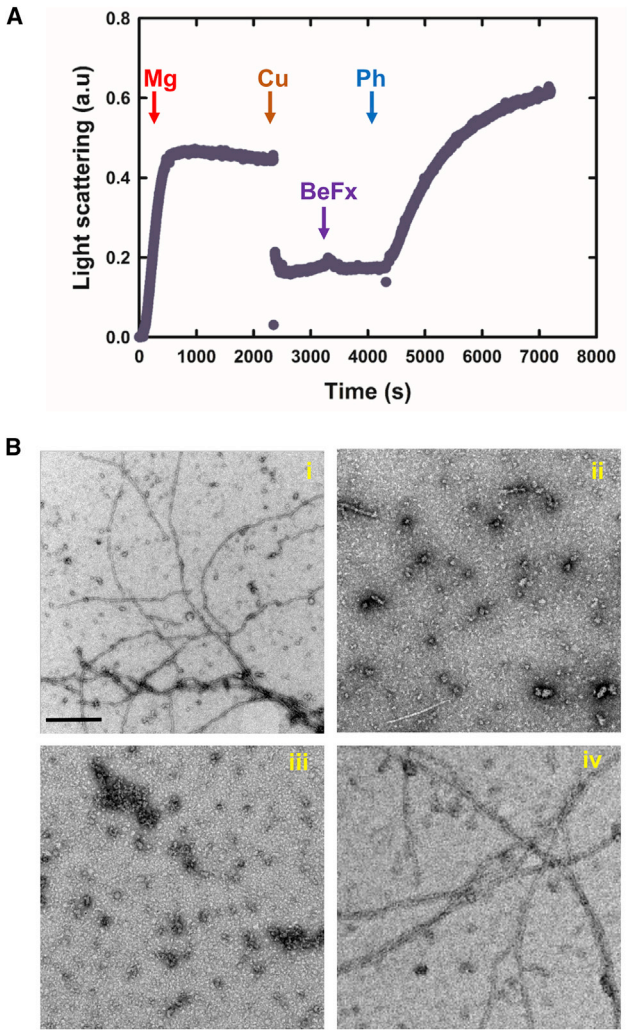

Figure 2. Phalloidin Rescues the Polymerization of Oxidized D-loop Actin Mutant C41/C45

(A) The polymerization of yeast actin mutant C41/C45 by 2 mM $MgCl_2$ was monitored by light-scattering measurements. At the polymerization plateau, 20 μM $CuSO_4$ was added to F-actin (orange arrow) to catalyze disulfide bond formation between C41 and C45. This resulted in filaments disassembly. Subsequent addition of BeFx (purple arrow) did not restore the filaments, but they were reformed upon addition of equimolar phalloidin (green arrow).

(B) Electron micrographs of C41/C45 actin collected after additions of: (i) Mg to G-actin, (ii) $CuSO_4$ to C41/C45 F-actin shown in (i), (iii) Mg followed by $CuSO_4$ and then followed by BeFx, and (iv) Mg, $CuSO_4$, BeFx, and phalloidin (in that order). EM samples were taken from experiments run in parallel to those shown in (A). For control filaments, 10 mM DTT was added to block disulfide bond formation. The scale bar in image (i) represents 0.2 μm.

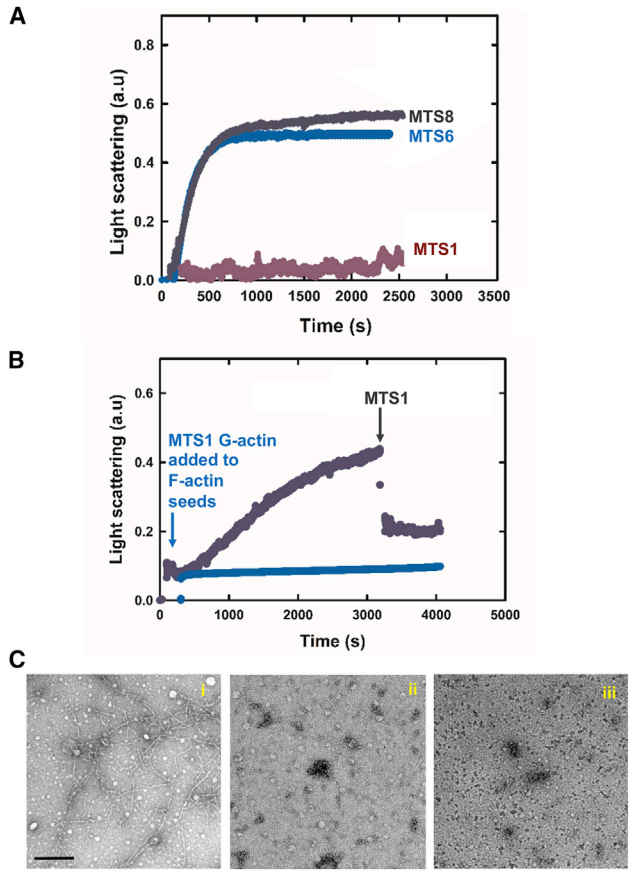

Figure 3. Crosslinking Span-Dependent Polymerization/Depolymerization of Actin D-loop Double Mutant C41/C45

(A) Yeast F-actin C41/C45 mutant was crosslinked with equimolar MTS1 (purple), MTS6 (blue), or MTS8 (gray) (with their mean respective crosslinking distances of ~5.4 Å, 10 Å, and 13 Å), and its polymerization by 2 mM $MgCl_2$ was monitored by light-scattering measurements.

(B) Yeast F-actin C41/C45 was depolymerized with the addition of equimolar MTS1. MTS1-crosslinked G-actin failed to polymerize in the presence of control actin filament seeds and 2 mM $MgCl_2$ (as monitored by light scattering).

(C) Electron micrographs of actin-C41/C45 after additions of: (i) MTS8 and Mg (filaments are formed); (ii) MTS1 and Mg (no filament formation); and (iii) MTS1 addition to F-actin (filaments are not detected). EM samples were taken from experiments ran in parallel to those shown in (A) and (B). The scale bar in EM images represents 0.2 μm.

filaments (Figures 2A and 2Bii), although they could be rescued by addition of phalloidin (Figures 2A, 2Biv, and S1) or 10 mM dithiothreitol (DTT) (not shown). In contrast to phalloidin, BeFx did not promote the polymerization of disulfide crosslinked actin (Figures 2A and 2Biii).

Comparison of helical D-loop in G-actin (Figure 1A) and in several F-actin (Figure 1B) structures showed flexibility in the D-loop region. Specifically, we measured the Cα-Cα distance between C41 and C45 for each structure and noticed a change in that distance between the G- and F-actin states (Figure 1C and Table S1). The two-dimensional interaction map using LigPlot+ (Laskowski and Swindells, 2011) of D-loop residues C41/C45 suggests how these residues interact with other domains of G- and F-actin in different nucleotide-bound states (Figures S2A–S2C) and in the presence of a bound phalloidin. Our structure-based analysis of the D-loop helped us to choose bifunctional methanethiosulfonate (MTS) reagents that were able to crosslink residues C41 to C45 at distances ranging from 5.4 Å (MTS1) to 13 Å (MTS8) (Figure 1D).

Our double-cysteine mutant of actin preincubated with MTS1 (span of ~5.4 Å) was unable to polymerize after addition of $MgCl_2$ (Figures 3A and 3Cii). To investigate whether this defect was due to elongation or nucleation inhibition, we supplemented the MTS1 experiment with seeds of uncrosslinked actin filaments.

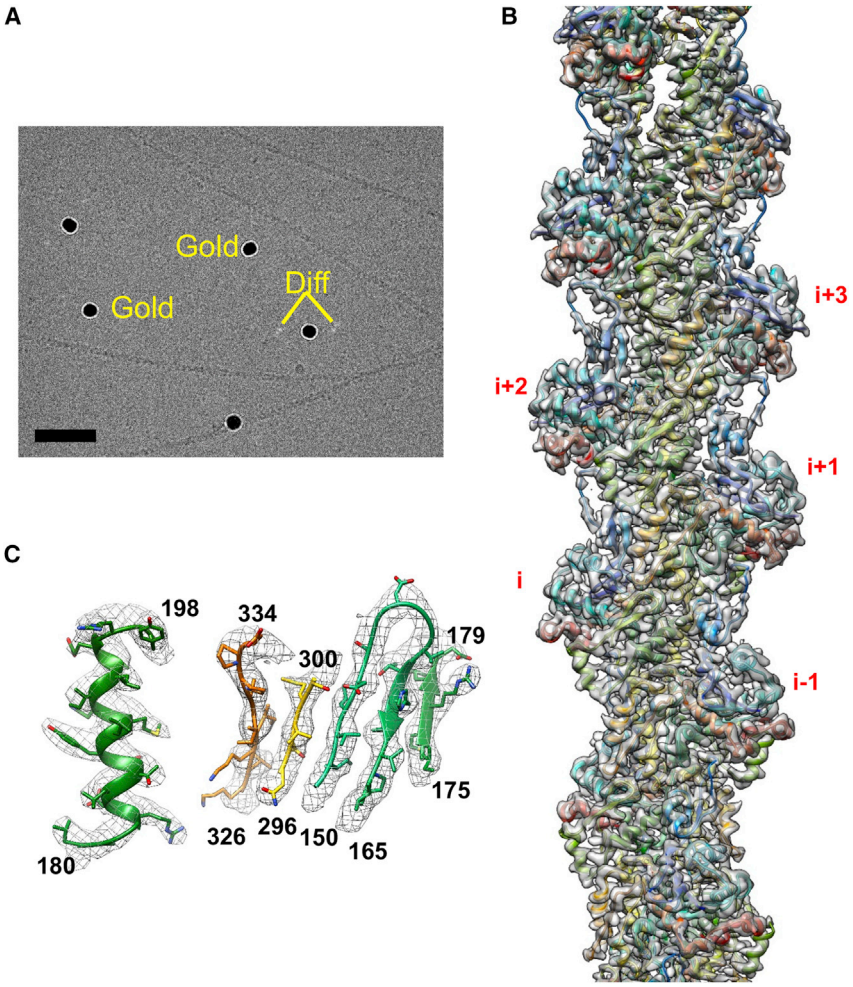

Figure 4. Cryo-EM Structure of ADP-BeFx-F-Actin-Phalloidin

(A) An average image of an aligned representative direct electron detector movie (stack). Gold, 10-nm gold particles; Diff, diffraction contrast generated by the lattice of gold particles. Scale bar, 400 Å.

(B) Overall structure of ADP-BeFx-F-actin-phalloidin at 3.3-Å resolution, fitted with atomic model of G-actin. Notations in red indicate the relative position of actin monomers in the filament.

(C) Representative regions (marked by amino acid numbers) of the density map fitted with their atomic models, showing the quality of the map.

Actin in (B) and (C) is shown in Chimera rainbow colors.

MTS1 crosslinked actin monomers failed to elongate from these seeds in the presence of Mg^{2+} (Figure 3B). We then tested other MTS crosslinkers, with increasing average arm length—MTS3 (span of ~6 Å), MTS6 (span of ~10 Å, Figure 3A), and MTS8 (span of ~13 Å, Figures 3A and 3Ci)—and monitored their ability to form polymers by light scattering and EM. Like MTS1-treated actin, MTS3 crosslinked monomers were unable to form filaments (not shown), but MTS6 (Figure 3A) and MTS8 (Figures 3A and 3Ci) crosslinked actin monomers readily polymerized into filaments. To test whether the change in crosslinking distance also affects filament stability, we first polymerized actin with 2 mM $MgCl_2$ under non-reducing conditions (Figure 3B) and then supplemented the reaction with equimolar MTS1 (Figure 3B) or MTS3 (data not shown). Addition of $CuSO_4$ (Figure 2A), MTS1, or MTS3 led to destruction of preformed filaments. When $CuSO_4$- or MTS1-treated samples were analyzed by negative stain, we saw no traces of actin filaments (Figures 2Bii and 3Ciii).

Cryo-EM of the Actin-Phalloidin Complex

We used high-resolution cryo-EM to obtain a three-dimensional structure of purified ADP-BeFx-F-actin in complex with phalloidin. The filaments appear straight and/or slightly curved in the collected images (Figure 4A). Despite the presence of unbound ligands and BeFx in the background, F-actin can be seen in the aligned and averaged stacks (Figure 4A). By using the iterative helical real-space refinement method (Egelman, 2010) implemented within the Relion 3 (He and Scheres, 2017) framework (Ge et al., 2014), we reconstructed a three-dimensional structure of F-actin at a resolution of 3.3 Å (Figures 4B, 4C, and S3). The map was reconstructed with about 156,000 asymmetric units selected from 5,873 direct electron detection movies (see STAR Methods). The refined helical parameter is different from previously reported ADP-BeFx (Merino et al., 2018) actin structures: the turn per subunit is 167.0° (versus 166.4° for ADP-actin and F-actin-Tm complex) (von der Ecken et al., 2015) and the rise per subunit is 27.57 Å. All α helices and β strands are well defined. Bound ligands and a large portion of the amino acid side chains are resolved in our density map (Figure 4C), permitting atomic modeling of both protein and its ligands. We built and refined to 3.3 Å an atomic model based on this cryo-EM map of F-actin and its bound ligands (Figures 4 and S3). The D-loop in this structure is elongated compared with others, making extra connections with neighboring subunits (Figure 5E and Video S1).

Phalloidin Stabilizes Actin by Bridging Protofilaments and Restricting Their Relative Movement

Phalloidin is a bicyclic heptapeptide, Ala-Trp-Leu $(OH)_2$-Ala-Thr-Cys-Pro (OH), with the sulfur atom of Cys covalently bound to the indole rings of Trp. Its density is well resolved in our map (Figure 5A). Phalloidin binds to F-actin in the cavity between three adjacent protomers, on the side opposite to the H-loop (Figure 5B and Video S2). It mainly interacts with two consecutive protomers. The heptapeptide is divided into four sections: one section (Leu$(OH)_2$-Ala-Thr) facing actin i, another (Ala-Trp) facing actin i + 1, its hydroxyproline facing the methylated His73, and its cysteine facing empty space between the protomers (Figures 5B–5D). Interactions between F-actin and phalloidin involve the first two sections of phalloidin. The first section of phalloidin interacts with loop 197–203 of actin i

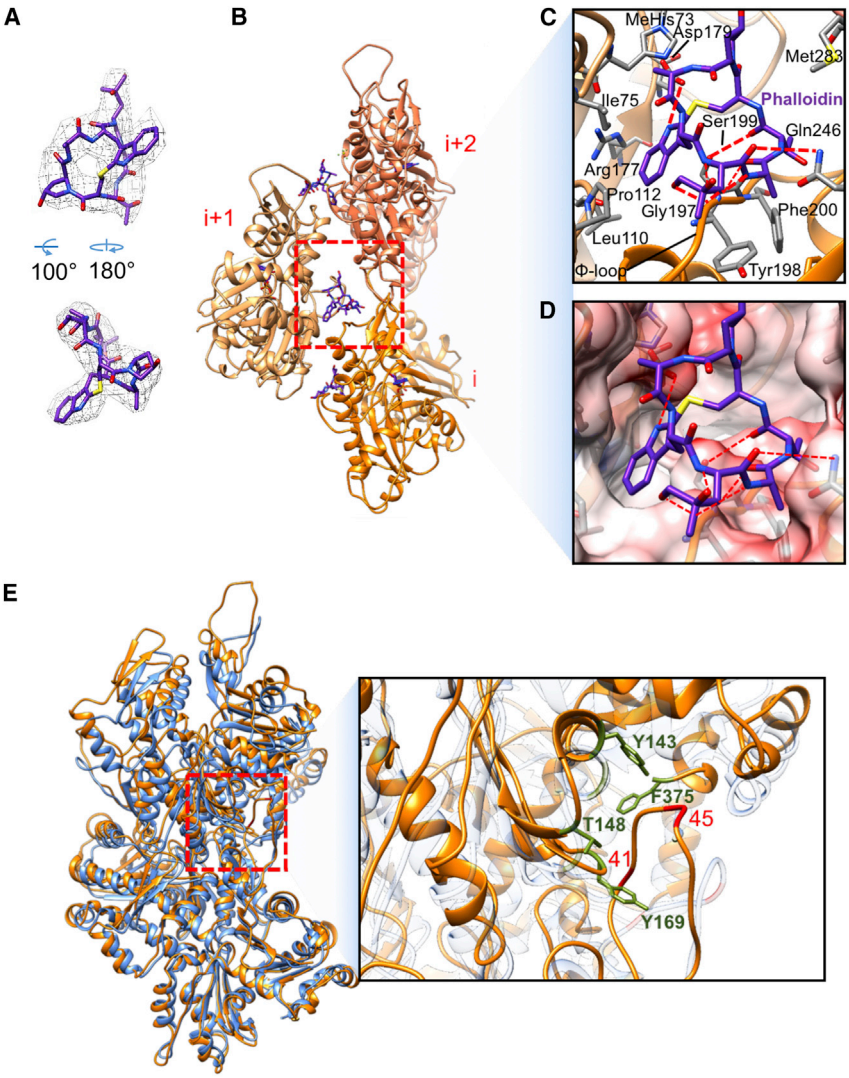

Figure 5. F-Actin Structure and Interactions with Phalloidin

(A) Chemical structure and atomic model of phalloidin (sticks) as resolved by our cryo-EM structure (mesh). The four sections of phalloidin are shown by colored blocks.

(B) Placement of phalloidin among actin protomers in the filament, with protomer units numbered in red.

(C and D) Close-up of interaction between phalloidin (sticks model) and actin (ribbon and stick in C, and molecular surface colored by Coulomb potential using Chimera in D). In all panels, the stick models for atoms are colored red for O, blue for N, and yellow for S; C atoms follow the color of the model. Hydrogen bonds are shown as red dotted lines.

(E) Phalloidin enhances inter-protomer D-loop contacts. To compare two D-loop regions, we superimposed ADP-BeFx-F-actin (PDB: 5OOF) on our ADP-BeFx-F-actin-phalloidin structure with Chimera. In the inset, a 3.5-Å zone around D-loop residues 41–45 was chosen with Chimera, and residues making contacts in our cryo-EM structure are shown by the stick option of Chimera. The published structure of BeFx-F-actin was made slightly transparent for visual clarity.

(phalloidin-binding loop, named the "Φ-loop") mainly through hydrophilic interactions (Figures 5C and 5D). The main chain of its alanine forms multiple hydrogen bonds (dotted lines in Figures 5C and 5D) with the main chain of Gly197-Ser199 of the Φ-loop reminiscent of an antiparallel β sheet. Hydrogen bonds between phalloidin and Gly197 and Glu246 reinforce this interaction. The second section, with the sulfur atom of the Cys of phalloidin, inserts into a hydrophobic pocket formed between actin i and i + 1. The interaction is mainly hydrophobic, except that Asp179 may form a hydrogen bond with the indole nitrogen of Trp.

DISCUSSION

The goal of this work has been to clarify the role of actin's D-loop dynamics and shape in filament assembly and stability. To this end, we used a double-cysteine mutant of D-loop, Q41C/V45C (with C374 mutated to S374), in crosslinkings of different span and assessed by light scattering and EM methods its ability to form filaments. The disabled assembly of actin with a short-span C41-to-C45 crosslinking was rescued by phalloidin. This prompted us to obtain a high-resolution cryo-EM structure of F-actin stabilized by phalloidin and BeFx and shed light on how phalloidin compensates for or overcomes local polymerization defects. The inclusion of both phalloidin and BeFx in F-actin was prompted by prior observations of their combined and additive stabilization of filaments as revealed in measurements of their persistence length (Isambert et al., 1995) and melting temperature (Levitsky et al., 2008). Because of the resolution of our cryo-EM maps, the electron density of BeFx is not identified in the presented images of actin filaments.

D-loop Is Dynamic and Has Several Structural States

To assess C41-to-C45 inter-residue distance changes that occur in different nucleotide-bound states of G- and F-actin (in our double mutant Q41C/V45C), we examined several high-resolution actin structures. A helical D-loop state has been reported in the crystal structure of uncomplexed ADP-bound G-actin (Otterbein et al., 2001). The Cα-Cα distance between residues 41 and 45 was 6.2 Å, but this increased to >11 Å in several F-actin structures (Figure S2D). It was speculated that this helix-to-loop change could be inherent to the transition between ATP and ADP nucleotide states of actin (Otterbein et al., 2001). The helical state of D-loop was not detected in other G-actin crystal structures, and thus the loop helix was ascribed to artifacts of crystal contacts (Rould et al., 2006). Yet MD simulations did show the formation of a D-loop helix (Pfaendtner et al., 2009), suggesting that its transient existence may be difficult to capture within current

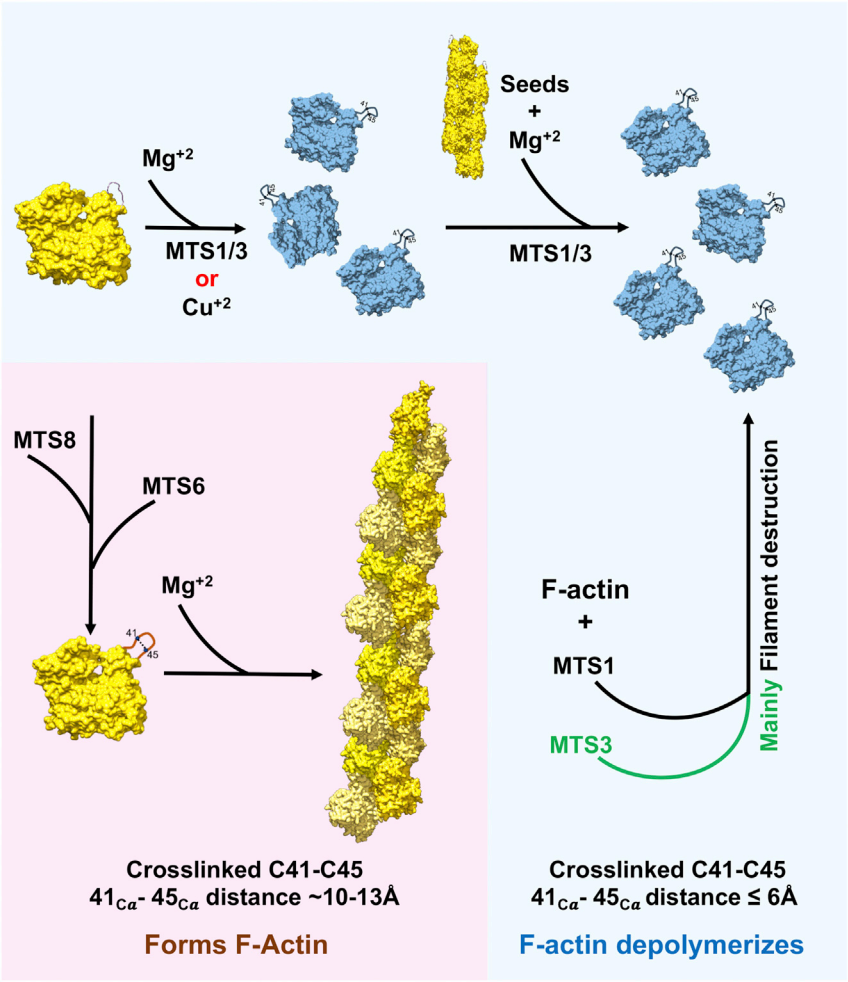

Figure 6. Model Representation of the Effects of Variable Distance Crosslinkings of C41 and C45 in Yeast Actin Mutant on Filament Formation or Destruction

detection methods. To test whether locking the double-cysteine mutant across a range of distances may play any significant role in actin dynamics, we utilized a distance-based crosslinking approach. Previously, MTS reagents were used as a molecular ruler to map distances between two cysteine residues placed in several domains of actin and in its D-loop (Oztug Durer et al., 2010). In our case, both disulfide and MTS1/3 crosslinked C41/C45 D-loop mutant was unable to nucleate actin filaments. Supplementing our reactions with F-actin seeds also failed to initiate their elongation. Furthermore, when polymerized mutant actin was treated with Cu^{2+} or MTS1/3, there was rapid filament destruction. Our results show that the filaments are disrupted or not formed when transient short separations of C41 and C45 (less than ~6 Å) are captured and locked by crosslinking. They imply also that if a helical state of D-loop exists, it must be transient. We did not observe any filament-disrupting effects when treating actin with MTS6 (~10 Å) or MTS8 (~13 Å) crosslinkers, indicating this to be a favorable separation of C41 and C45 that allows filament formation and stability.

Our results are also consistent with several reported states of D-loop in high-resolution F-actin structures. They suggest changes that can be attributed to a dynamic nature of the filament, and support an open and extended D-loop compared with that in G-actin. Previous biochemical and structural studies support that conclusion. Notable is a striking contrast between the filament-disruptive effect of short-range crosslinking of amino acids 41–45 (shown in the present work) versus only a minor perturbation of actin polymerization and interactions with myosin following a zero-length crosslinking of Q41 to K50 on actin by transglutaminase (Eli-Berchoer et al., 2000). This latter crosslinking does not constrain the open nature of the D-loop. Consistent with this, electron paramagnetic resonance (EPR) studies and acrylodan labeling experiments suggested that D-loop residues 41, 42, 49, and 50 participate less extensively in filament contacts (Durer et al., 2012). Moreover, EPR experiments with yeast actin and its D-loop residues labeled with spin probes showed their multiple states and mobility, and revealed partial immobilization in F-actin of the probes attached mainly to amino acids 43–47 (Durer et al., 2012). Combined, the present and past results attest to F-actin preference for the open state of the D-loop.

Phalloidin Stabilizes Actin Filaments by Inter-subunit Contacts

In recent years direct electron counting has revolutionized cryo-EM analysis of biological samples. This has led to several high-resolution maps (3.2–4.6 Å) of F-actin structure (Merino et al., 2018; Chou and Pollard, 2019; Gurel et al., 2017), but some important questions about them remain open. Here, we use high-resolution cryo-EM and ADP-BeFx-F-actin-phalloidin to map phalloidin's binding site on actin filaments and reveal how it restricts the relative movement between their two strands and stabilizes F-actin structure. We document important intermolecular contacts in F-actin that are consistent with other high-resolution structures. Although the interaction among protomers along a single filament strand is relatively strong in the ADP-Pi state (Chou and Pollard, 2019), the two protomers attach to each other with merely two salt bridges: Glu270 of H-loop with Arg39 of D-loop and Glu195 near Φ-loop and Lys113. This configuration is conducive to a variable twist: rectangular structures are prone to shearing or twisting forces. Phalloidin restricts this variability by adding struts that form triangles,

which are not easily deformed by such forces. Phalloidin binds actin with a high binding constant of $(1.5 + 0.11) \times 10^8$ M^{-1} (De La Cruz and Pollard, 1996). It is likely that its bicyclic structure largely limits its degrees of freedom and thus compensates for torsional free energy.

On average, each phalloidin molecule has 760 $Å^2$ of surface area buried within actin, almost doubling the inter-protofilament contact (919 $Å^2$ per protomer). This explains how it rescues the assembly of many actin mutants that are defective in their polymerization, as seen here (Figure 2A) and in previous studies (Oztug Durer et al., 2010). We hypothesize that by creating such contacts phalloidin acts as a "superglue" connecting three actin protomers, thereby stabilizing the filament and bypassing the D-loop anomaly. Our actin-phalloidin structure also reveals additional conformational changes in the D-loop compared with the ADP-BeFx-F-actin structure (Merino et al., 2018) (Figure 5E), causing it to extend and establish contacts with residues Tyr148, Thr143, Tyr169, and the C-terminal Phe375 of the neighboring actin. Our structure is consistent with a previous high-resolution actomyosin structure stabilized by phalloidin. The location of phalloidin and the contacts formed by most of the interacting residues are comparable. However, in actomyosin complex phalloidin forms additional contacts compared with those seen in our structure. Those additional interactions may be due to F-actin stabilization by myosin (Mentes et al., 2018). Our structure is also consistent with the study of phalloidin-actin complex structure (Pospich et al., 2020), which became available as this paper was undergoing revision.

Taken together, our results provide a model (Figure 6) of preferred D-loop state in F-actin based on inter-residue distance-dependent changes in actin polymerization and filament stability. We show how locking the D-loop residues below an optimal distance between them blocks the transition between G- and F-actin. The fact that intra-loop short-span crosslinkings can occur between amino acids 41 and 45 in F-actin, which result in rapid filament destruction, attests to the dynamic nature of D-loop in the filaments. In addition, the high-resolution structure of actin-phalloidin reveals additional contacts made by phalloidin that stabilize actin filaments and help to incorporate polymerization-defective monomer units in the filaments.

STAR★METHODS

Detailed methods are provided in the online version of this paper and include the following:

- KEY RESOURCES TABLE
- RESOURCE AVAILABILITY
  - Lead Contact
- MATERIALS AVAILABILITY
  - Data and Code Availability
- EXPERIMENTAL MODEL AND SUBJECT DETAILS
- METHOD DETAILS
  - Purification of Yeast Actin Mutants
  - MTS Cross-linking and Light Scattering
  - Negative Stain Electron Microscopy
  - CryoEM
  - Image Processing and Atomic Modeling
- QUANTIFICATION AND STATISTICAL ANALYSIS

SUPPLEMENTAL INFORMATION

Supplemental Information can be found online at https://doi.org/10.1016/j.str.2020.04.004.

ACKNOWLEDGMENTS

We thank Pamchal Faroghi and Zixin Zhang for assistance with yeast actin preparation. We also thank Zixin Zhang, Raul Soto Jr., and Saichandra Kalvakota for assistance with Tecan and gel-electrophoresis experiments. This work was supported by grants from the National Institutes of Health to E.R. (GM077190) and Z.H.Z. (AI094386 and GM071940), and the American Heart Association Postdoctoral Fellowship to P.G. (13POST17340020). We acknowledge the use of instruments at the Electron Imaging Center for Nanomachines supported by UCLA and by instrumentation grants from NIH (1S10RR23057, 1S10OD018111) and NSF (DBI-1338135). The content is solely the responsibility of the authors and does not necessarily reflect the official views of the National Institute of General Medical Sciences or the NIH.

AUTHOR CONTRIBUTIONS

Conceptualization, S.D., P.G., and E.R.; Methodology, S.D., P.G., E.E.G., Z.A.O.D, Z.H.Z., and E.R.; Experimentation, S.D., P.G., E.E.G., and Z.A.O.D. Writing, S.D., P.G., E.E.G., Z.H.Z., and E.R.; Visualization, S.D. and P.G.; Supervision, E.R.; Funding Acquisition, E.R., P.G., and Z.H.Z.

DECLARATION OF INTERESTS

The authors declare no competing interests.

Received: August 27, 2019
Revised: February 28, 2020
Accepted: April 6, 2020
Published: April 28, 2020

REFERENCES

Adams, P.D., Afonine, P.V., Bunkóczi, G., Chen, V.B., Davis, I.W., Echols, N., Headd, J.J., Hung, L.-W., Kapral, G.J., Grosse-Kunstleve, R.W., et al. (2010). PHENIX: a comprehensive Python-based system for macromolecular structure solution. Acta Crystallogr. D Biol. Crystallogr. *66*, 213–221.

Campbell, M.G., Cheng, A., Brilot, A.F., Moeller, A., Lyumkis, D., Veesler, D., Pan, J., Harrison, S.C., Potter, C.S., Carragher, B., et al. (2012). Movies of ice-embedded particles enhance resolution in electron cryo-microscopy. Structure *20*, 1823–1828.

Chou, S.Z., and Pollard, T.D. (2019). Mechanism of actin polymerization revealed by cryo-EM structures of actin filaments with three different bound nucleotides. Proc. Natl. Acad. Sci. U S A *116*, 4265–4274.

Dalhaimer, P., Pollard, T.D., and Nolen, B.J. (2008). Nucleotide-mediated conformational changes of monomeric actin and Arp3 studied by molecular dynamics simulations. J. Mol. Biol. *376*, 166–183.

Dominguez, R., and Holmes, K.C. (2011). Actin structure and function. Annu Rev Biophys. *40*, 169–186.

Durer, Z.A.O., Kudryashov, D.S., Sawaya, M.R., Altenbach, C., Hubbell, W., and Reisler, E. (2012). Structural states and dynamics of the D-loop in actin. Biophys. J. *103*, 930–939.

von der Ecken, J., Müller, M., Lehman, W., Manstein, D.J., Penczek, P.A., and Raunser, S. (2015). Structure of the F-actin–tropomyosin complex. Nature *519*, 114–117.

Egelman, E.H. (2010). Reconstruction of helical filaments and tubes. Methods Enzymol. *482*, 167–183.

Eli-Berchoer, L., Reisler, and Muhlrad. (2000). Effect of intramolecular cross-linking between glutamine-41 and lysine-50 on actin structure and function. J. Muscle Res. Cell Motil. *78*, 405–414.

Emsley, P., and Cowtan, K. (2004). Coot: model-building tools for molecular graphics. Acta Crystallogr. D Biol. Crystallogr. *60*, 2126–2132.

Galkin, V.E., Orlova, A., Vos, M.R., Schröder, G.F., and Egelman, E.H. (2015). Near-atomic resolution for one state of F-actin. Structure *23*, 173–182.

Ge, P., Durer, Z.A.O., Kudryashov, D., Zhou, Z.H., and Reisler, E. (2014). Cryo-EM reveals different coronin binding modes for ADP- and ADP-BeFx actin filaments. Nat. Struct. Mol. Biol. *21*, 1075–1081.

Graceffa, P., and Dominguez, R. (2003). Crystal structure of monomeric actin in the ATP state. Structural basis of nucleotide-dependent actin dynamics. J. Biol. Chem. *278*, 34172–34180.

Grintsevich, E.E., Ge, P., Sawaya, M.R., Yesilyurt, H.G., Terman, J.R., Zhou, Z.H., and Reisler, E. (2017). Catastrophic disassembly of actin filaments via Mical-mediated oxidation. Nat. Commun. *8*, 2183.

Gurel, P.S., Kim, L.Y., Ruijgrok, P.V., Omabegho, T., Bryant, Z., and Alushin, G.M. (2017). Cryo-EM structures reveal specialization at the myosin VI-actin interface and a mechanism of force sensitivity. eLife *6*, https://doi.org/10.7554/eLife.31125.

He, S., and Scheres, S.H.W. (2017). Helical reconstruction in RELION. J. Struct. Biol. *198*, 163–176.

Isambert, H., Venier, P., Maggs, A.C., Fattoum, A., Kassab, R., Pantaloni, D., and Carlier, M.F. (1995). Flexibility of actin filaments derived from thermal fluctuations. Effect of bound nucleotide, phalloidin, and muscle regulatory proteins. J. Biol. Chem. *270*, 11437–11444.

Kabsch, W., Mannherz, H.G., Suck, D., Pai, E.F., and Holmes, K.C. (1990). Atomic structure of the actin:DNase I complex. Nature *347*, 37–44.

Kim, E., and Reisler, E. (1996). Intermolecular coupling between loop 38-52 and the C-terminus in actin filaments. Biophys. J. *71*, 1914–1919.

Kim, E., Phillips, M., Hegyi, G., Muhlrad, A., and Reisler, E. (1998). Intrastrand cross-linked actin between Gln-41 and Cys-374. II. Properties of cross-linked oligomers. Biochemistry *37*, 17793–17800.

Kotila, T., Kogan, K., Enkavi, G., Guo, S., Vattulainen, I., Goode, B.L., and Lappalainen, P. (2018). Structural basis of actin monomer re-charging by cyclase-associated protein. Nat. Commun. *9*, 1892.

De La Cruz, E.M., and Pollard, T.D. (1996). Kinetics and thermodynamics of phalloidin binding to actin filaments from three divergent species. Biochemistry *35*, 14054–14061.

Laskowski, R.A., and Swindells, M.B. (2011). LigPlot+: multiple ligand–protein interaction diagrams for drug discovery. J. Chem. Inf. Model. *51*, 2778–2786.

Levitsky, D.I., Pivovarova, A.V., Mikhailova, V.V., and Nikolaeva, O.P. (2008). Thermal unfolding and aggregation of actin: stabilization and destabilization of actin filaments. FEBS J. *275*, 4280–4295.

Li, X., Mooney, P., Zheng, S., Booth, C.R., Braunfeld, M.B., Gubbens, S., Agard, D.A., and Cheng, Y. (2013). Electron counting and beam-induced motion correction enable near-atomic-resolution single-particle cryo-EM. Nat. Methods *10*, 584–590.

McLaughlin, P.J., Gooch, J.T., Mannherz, H.G., and Weeds, A.G. (1993). Structure of gelsolin segment 1-actin complex and the mechanism of filament severing. Nature *364*, 685–692.

Mentes, A., Huehn, A., Liu, X., Zwolak, A., Dominguez, R., Shuman, H., Ostap, E.M., and Sindelar, C.V. (2018). High-resolution cryo-EM structures of actin-bound myosin states reveal the mechanism of myosin force sensing. Proc. Natl. Acad. Sci. U S A *115*, 1292–1297.

Merino, F., Pospich, S., Funk, J., Wagner, T., Küllmer, F., Arndt, H.-D., Bieling, P., and Raunser, S. (2018). Structural transitions of F-actin upon ATP hydrolysis at near-atomic resolution revealed by cryo-EM. Nat. Struct. Mol. Biol. *25*, 528–537.

Neuhaus, J.M., Wanger, M., Keiser, T., and Wegner, A. (1983). Treadmilling of actin. J. Muscle Res. Cell Motil. *4*, 507–527.

Oda, T., Namba, K., and Maéda, Y. (2005). Position and orientation of phalloidin in F-actin determined by X-ray fiber diffraction analysis. Biophys. J. *88*, 2727–2736.

Oda, T., Iwasa, M., Aihara, T., Maéda, Y., and Narita, A. (2009). The nature of the globular- to fibrous-actin transition. Nature *457*, 441–445.

Orlova, A., and Egelman, E.H. (1992). Structural basis for the destabilization of F-actin by phosphate release following ATP hydrolysis. J. Mol. Biol. *227*, 1043–1053.

Otterbein, L.R., Graceffa, P., and Dominguez, R. (2001). The crystal structure of uncomplexed actin in the ADP state. Science *293*, 708–711.

Orlova, A., and Egelman, E.H. (1993). A conformational change in the actin subunit can change the flexibility of the actin filament. J Mol Biol *232*, 334–341.

Oztug Durer, Z.A., Diraviyam, K., Sept, D., Kudryashov, D.S., and Reisler, E. (2010). F-actin structure destabilization and DNase I binding loop: fluctuations mutational cross-linking and electron microscopy analysis of loop states and effects on F-actin. J. Mol. Biol. *395*, 544–557.

Paavilainen, V.O., Bertling, E., Falck, S., and Lappalainen, P. (2004). Regulation of cytoskeletal dynamics by actin-monomer-binding proteins. Trends Cell Biol. *14*, 386–394.

Pettersen, E.F., Goddard, T.D., Huang, C.C., Couch, G.S., Greenblatt, D.M., Meng, E.C., and Ferrin, T.E. (2004). UCSF Chimera: a visualization system for exploratory research and analysis. J. Comput. Chem. *25*, 1605–1612.

Pfaendtner, J., Branduardi, D., Parrinello, M., Pollard, T.D., and Voth, G.A. (2009). Nucleotide-dependent conformational states of actin. Proc. Natl. Acad. Sci. U S A *106*, 12723–12728.

Pollard, T.D. (2016). Actin and actin-binding proteins. Cold Spring Harb. Perspect. Biol. *8*, https://doi.org/10.1101/cshperspect.a018226.

Pollard, T.D. (2017). What we know and do not know about actin. Handb. Exp. Pharmacol. *235*, 331–347.

Pospich, S., Merino, F., and Raunser, S. (2020). Structural effects and functional implications of phalloidin and jasplakinolide binding to actin filaments. Structure *28*, 437–449.e5.

Robinson, R.C., Mejillano, M., Le, V.P., Burtnick, L.D., Yin, H.L., and Choe, S. (1999). Domain movement in gelsolin: a calcium-activated switch. Science *286*, 1939–1942.

Rould, M.A., Wan, Q., Joel, P.B., Lowey, S., and Trybus, K.M. (2006). Crystal structures of expressed non-polymerizable monomeric actin in the ADP and ATP states. J. Biol. Chem. *281*, 31909–31919.

Saunders, M.G., Tempkin, J., Weare, J., Dinner, A.R., Roux, B., and Voth, G.A. (2014). Nucleotide regulation of the structure and dynamics of G-actin. Biophys. J. *106*, 1710–1720.

Schindelin, J., Arganda-Carreras, I., Frise, E., Kaynig, V., Longair, M., Pietzsch, T., Preibisch, S., Rueden, C., Saalfeld, S., Schmid, B., et al. (2012). Fiji: an open-source platform for biological-image analysis. Nat. Methods *9*, 676–682.

Shvetsov, A., Stamm, J.D., Phillips, M., Warshaviak, D., Altenbach, C., Rubenstein, P.A., Hideg, K., Hubbell, W.L., and Reisler, E. (2006). Conformational dynamics of loop 262-274 in G- and F-actin. Biochemistry *45*, 6541–6549.

Spudich, J.A., and Watt, S. (1971). The regulation of rabbit skeletal muscle contraction. I. biochemical studies of the interaction of the tropomyosin-troponin complex with actin and the proteolytic fragments of myosin. J Biol Chem. *246*, 4866–4871.

Suarez, C., Roland, J., Boujemaa-Paterski, R., Kang, H., McCullough, B.R., Reymann, A.-C., Guérin, C., Martiel, J.-L., De La Cruz, E.M., and Blanchoin, L. (2011). Cofilin tunes the nucleotide state of actin filaments and severs at bare and decorated segment boundaries. Curr. Biol. *21*, 862–868.

Tang, G., Peng, L., Baldwin, P.R., Mann, D.S., Jiang, W., Rees, I., and Ludtke, S.J. (2007). EMAN2: an extensible image processing suite for electron microscopy. J. Struct. Biol. *157*, 38–46.

Tirion, M.M., and ben-Avraham, D. (1993). Normal mode analysis of G-actin. J. Mol. Biol. *230*, 186–195.

Zheng, X., Diraviyam, K., and Sept, D. (2007). Nucleotide effects on the structure and dynamics of actin. Biophys. J. *93*, 1277–1283.

STAR★METHODS

KEY RESOURCES TABLE

REAGENT or RESOURCE	SOURCE	IDENTIFIER
Chemicals, Peptides, and Recombinant Proteins		
Uranyl Formate	EM Sciences	Cat# 22450
1,1-Methanediyl Bismethanethiosulfonate (MTS-1)	Toronto Research Chemicals	Cat# M258800
1,3-Propanediyl Bismethanethiosulfonate (MTS-3)	Toronto Research Chemicals	Cat# P760350
1,6-Hexanediyl Bismethanethiosulfonate (MTS-6)	Toronto Research Chemicals	Cat# H294250
1,8-Octadiyl Bismethanethiosulfonate (MTS-8)	Toronto Research Chemicals	Cat#O235850
Deoxyribonuclease I (DNase I)	Worthington Biochemical	Cat# LS002139
Affi-Gel 10 Gel	BioRad	Cat# 1536099
Deposited Data		
Actin phalloidin at BeFx state	This paper	PDB: 6U96
Actin phalloidin at BeFx state	This paper	EMDB: 20694
F-actin in complex with ADP-BeFx	Merino et al.,2018	PDB: 5OOF
Uncomplexed actin in the ADP state	Otterbein et al., 2001	PDB: 1J6Z
Structure of ADP-actin filaments	Chou and Pollard, 2019	PDB: 6DJO
Structure of AMPPNP-actin filaments	Chou and Pollard, 2019	PDB: 6DJM
Experimental Models: Organisms/Strains		
Saccharomyces cerevisiae C4145 mutant strain in pRS314	Dr. Reisler's lab, this paper	C41-C45
Software and Algorithms		
CHIMERA	Pettersen et al., 2004	https://www.cgl.ucsf.edu/chimera/download.html
RELION 3.0	He and Scheres, 2017	https://www3.mrc-lmb.cam.ac.uk/relion
Coot	Emsley and Cowtan, 2004	https://www2.mrc-lmb.cam.ac.uk/personal/pemsley/coot/
MotionCorr	Li et al., 2013	https://emcore.ucsf.edu/ucsf-motioncor2
Phenix	Adams et al., 2010	https://www.phenix-online.org/
ImageJ	Schindelin et al., 2012	https://imagej.net/ImageJ
EMAN	Tang et al.,2007	http://blake.bcm.tmc.edu/EMAN2/
Sigmaplot14	Systat Software, Inc., San Jose California USA	https://systatsoftware.com/products/sigmaplot/
LigPlot+	Laskowski and Swindells, 2011	https://www.ebi.ac.uk/thornton-srv/software/LigPlus/
Other		
Gilder Copper grids, 400 Mesh	Ted Pella	Cat#G400

RESOURCE AVAILABILITY

Lead Contact

Further information and requests for resources and reagents should be directed to and will be fulfilled by the Lead Contact, Emil Reisler (reisler@mbi.ucla.edu).

MATERIALS AVAILABILITY

This study did not generate new unique reagents.

CellPress

Data and Code Availability

3D cryoEM density map has been deposited in the Electron Microscopy Data Bank under the accession number EMD-20694. The coordinates of atomic model have been deposited in the Protein Data Bank under the accession number PDB: 6U96. This study did not generate any new code.

EXPERIMENTAL MODEL AND SUBJECT DETAILS

Saccharomyces cerevisiae C4145 actin mutant strain in pRS314 was used for protein expression and purification (Oztug Durer et al., 2010). In this study the double D-loop mutant has also a C374A mutation.

METHOD DETAILS

Purification of Yeast Actin Mutants

Yeast actin was purified essentially as described earlier (Oztug Durer et al., 2010). The protein was eluted from a DNase I affinity column with buffer A (10 mM Tris (pH 7.8), 1 mM DTT, 0.2 mM ATP, and 0.2 mM $CaCl_2$) containing 20-25% sucrose and 50% formamide, and was then applied directly to a DEAE column. Actin was eluted from the DEAE column in the same buffer containing 350 mM KCl. Purified G-actin was cycled,dialyzed and stored in buffer B (10 mM HEPES (pH ~7.4), 0.2 mM $CaCl_2$, 0.2 mM ATP, 1.0 mM DTT) on ice.

MTS Cross-linking and Light Scattering

Prior to cross-linking the protein was dialyzed in buffer B supplemented with 0.25mM DTT for ~2 hours followed by 0.1mM DTT for an hour. Immediately after dialysis DTT was removed completely by passing actin through Sephadex G-50 spin columns equilibrated with buffer B (no DTT). The recovered G-actin was then used in the experiments. Actin polymerization, and its disruption due to disulfide cross-linking was monitored via light scattering measurements with the PTI fluorometer (with the excitation and emission wavelengths set at 325nm). Actin polymerization was induced by adding 2.0 mM $MgCl_2$ to G-actin (6.0 μM). Equimolar ratios of phalloidin and MTS reagents to actin, and 2:1 ratio of $CuSO_4$ to actin were added as indicated in figure legends.

Negative Stain Electron Microscopy

Samples collected at various time points were applied to 400-mesh carbon-coated copper grids coated with formvar films (EM Sciences). After 60 seconds of adsorption, the grids were blotted dry and treated with 1% uranyl acetate for 45 seconds. The grids were examined in a Technai T12 electron microscope operated at 120 kV. The collected images were analyzed by using IMAGE J (Schindelin et al., 2012) software.

CryoEM

For cryo electron microscopy (cryoEM) samples of skeletal actin were polymerized for 1 h on ice in a buffer containing: 10mM Tris, pH7.4, 0.2mM $CaCl_2$, 50mM KCl, 1.05mM $MgCl_2$, 1mM ATP, 1mM DTT, 0.2mM EGTA. This buffer was supplemented with BeFx (0.2mM $BeCl_2$, 5mM NaF) and equimolar ratio of phalloidin to actin to stabilize the filaments. Skeletal actin was prepared as described earlier (Spudich and Watt, 1971).

Aliquots of 2.5 μL of several F-actin samples were applied onto a "baked" 33 Quantifoil 1.2/1.3 μm, 200 mesh grid, blotted for 4.5 seconds at force 1, then flash-frozen in liquid nitrogen-cooled liquid ethane in a Vitrobot Mark IV (FEI). Grids with frozen-hydrated F-actin were loaded into an FEI Titan Krios electron microscope operated at 300 kV for semi-automated image acquisition with Leginon. CryoEM micrographs were recorded on a Gatan K2 Summit direct electron detector camera using the electron counting mode at 130,000x nominal magnification (calibrated pixel size of 1.07 Å on the sample level) and defocus values ranging from 2.2 – 4.2 μm. The dose rate on the camera was set to ~8 $e/A^2/s$. The total exposure time was 8 s, which is fractionated into 32 frames, with 0.25 s exposure time for each frame. We recorded movies (Campbell et al., 2012) of this actin sample with the K2 direct electron detector. Because of the small diameter of F-actin, and the use of 300 keV electrons in cryoEM imaging, individual frames of direct electron counting movies do not have sufficient signal to be aligned directly. Therefore, we added 10 nm gold particles to the sample, which are prominently visible in Figure 4A, in order to generate a fiducial signal for frame alignment. The gold particles and Fresnel fringes around them enabled us to align the individual frames in most of the movies and to determine their defocus parameters.

Image Processing and Atomic Modeling

The movies were aligned and averaged for correction of beam-induced drift using the GPU-accelerated program MotionCorr (Li et al., 2013). The average images from all frames were used for defocus determination and particle picking, and those from the first 16 frames (corresponding to ~30 $e^-/Å^2$ total dose on sample) were aligned and summed to produce a micrograph for 2D and 3D image classification. From the total of 5,874 movies recorded in a continuous session, we selected the best 2,865 micrographs for in-depth data processing.

We manually picked 6,761 actin segments from selected micrographs by EMAN (Tang et al., 2007) helixboxer, and segmented them into 214,583 boxes of 360x360 pixels by 10% interbox distance. We used Relion Class2D and Class3D to eliminate bad particles. The Iterative Helical Real-Space Refinement (IHRSR) method (Egelman, 2010) as implemented within the Relion 3 (He and

Scheres, 2017) framework was used to process the selected particles for high-resolution reconstruction. The final, helical cryoEM density map was calculated from 181,627 selected particles with Refine3D, to a resolution of 3.8 Å. We then re-extracted sub-particles (96x96 boxes) from these selected particles and finely adjusted their orientation and center parameters locally. The resolution of the newly reconstructed, sub-particle map was determined to be 3.3 Å based on the "gold-standard" FSC criterion. Atomic model of actin was initially built with Coot (Emsley and Cowtan, 2004) and refined with Phenix real_space_refine (Adams et al., 2010).

QUANTIFICATION AND STATISTICAL ANALYSIS

Graphs were plotted using Sigmaplot v14 (from Systat Software, Inc., San Jose California USA, www.systatsoftware.com). Figures containing CryoEM map and model were generated using Chimera (Pettersen et al., 2004). All biochemical experiments were repeated for at least 3 times (n3).